Journal of Nuclear Materials 393 (2009) 254–266

Contents lists available at ScienceDirect

Journal of Nuclear Materials

journal homepage: www.elsevier.com/locate/jnucmat

Advanced TEM characterization of stress corrosion cracking of Alloy 600 in pressurized water reactor primary water environment

M. Sennour [a,*], P. Laghoutaris [a,b], C. Guerre [b], R. Molins [a]

[a] MINES ParisTech, Centre des Matériaux, UMR CNRS 7633, B.P. 87 91003 Evry Cedex, France
[b] CEA, DEN, DPC, SCCME Laboratoire d'Etude de la Corrosion Aqueuse, F – 91191 Gif sur Yvette Cedex, France

ARTICLE INFO

Article history:
Received 14 January 2009
Accepted 15 June 2009

PACS:
68.37.−d
28.41.Fr
81.40.Np
62.20.mt

ABSTRACT

Advanced transmission electron microscopy techniques were carried out in order to investigate stress corrosion cracking in Alloy 600 U-bend samples exposed in simulated PWR primary water at 330 °C. Using high-resolution imaging and fine-probe chemical analysis methods, ultrafine size oxides present inside cracks and intergranular attacks were nanoscale characterized. Results revealed predominance of Cr_2O_3 oxide and Ni-rich metal zones at the majority of encountered crack tip areas and at leading edge of intergranular attacks. However, NiO-structure oxide was predominant far from crack tip zones and within cracks propagating along twin boundaries and inside grains. These observations permit to suggest a mechanism for intergranular stress corrosion cracking of Alloy 600 in PWR primary water. Indeed, the results suggest that stress corrosion cracking is depending on chromium oxide growth in the grain boundary. Oxide growth seems to be dependent on oxygen diffusion in porous oxide and chromium diffusion in strained alloy and in grain boundary beyond crack tip. Strain could promote transport kinetic and oxide formation by increasing defaults rate like dislocations.

1. Introduction

Alloy 600, a nickel base alloy (containing 15 wt% Cr) used in primary coolant circuits of pressurized water reactors (PWR), is susceptible to intergranular stress corrosion cracking (IGSCC). Despite the fact that many laboratory studies were performed and that many models were proposed in the literature [1–4], the stress corrosion cracking (SCC) mechanisms involved are still not well understood. Among other models, the internal oxidation model [5] and models based on hydrogen/material interactions [6,7] appear likely to explain this phenomenon.

In order to understand SCC, advanced characterization techniques are necessary to provide information approaching the atomic scale. Studies involving analytical transmission electron microscopy (ATEM), analysis of SCC and intergranular attack (IGA) in Alloy 600 have been reported in the literature [8,9]. These investigations suggest that oxidation or dissolution process control SCC in PWR conditions. Nevertheless, they could not discriminate the SCC mechanism.

The present study aims to get new information and data in order to understand SCC mechanisms of Alloy 600 in PWR primary water. As SCC involves phenomena which are active at nanometre scale, advanced methods of high-resolution analytical transmission electron microscopy were carried out in order to investigate nature of ultrafine size oxides formed at crack tips and intergranular attack (IGA) leading edge areas. The present paper describes microstructural investigations performed on U-bends samples machined in two different heats of Alloy 600 and tested in nominal PWR primary water at 330 °C. The comparison between both heats permits to characterize the influence of intergranular precipitation which is well known to play a significant role on SCC susceptibility [10].

2. Experimental

2.1. Materials and corrosion test

Two mill annealed (MA) Alloy 600 heats (NX2650 MA, NX3332 MA) were used in this study. The corresponding compositions are given in Table 1 and both heats general microstructure are shown in Fig. 1.

U-bend samples for the corrosion test were prepared by cutting tubes longitudinally into four pieces and flattening the pieces using a hydraulic press. The original inner tube surface is the outer surface of the U-bend. Stresses at the apex of the U-bend were evaluated by X-ray diffraction measurements from 650 MPa to 725 MPa and 300 MPa to 500 MPa in the original longitudinal and transverse axes, respectively.

Corrosion testing was performed in an isothermal loop at 330 °C and a pressure of 15 MPa. The flow rate was 25–27 m^3/h with 0.1% of the flow continuously purified. Simulated nominal PWR primary

---

[*] Corresponding author. Tel.: +331 6076 3107; fax: +331 6076 3150.
E-mail address: mohamed.sennour@ensmp.fr (M. Sennour).

0022-3115/$ - see front matter © 2009 Elsevier B.V. All rights reserved.
doi:10.1016/j.jnucmat.2009.06.014

Table 1
Heats composition (wt%).

Heats	C	Si	S	P	Mn	Ni	Cr	Cu	Co	Ti	Al	Fe
NX 2650	0.038	0.21	0.001	0.008	0.3	74.83	15.06	0.29	0.05	0.22	0.24	9.27
NX 3332	0.032	0.12	0.005	0.009	0.26	74.48	16.1	0.125	0.033	0.1	0.1	8.63

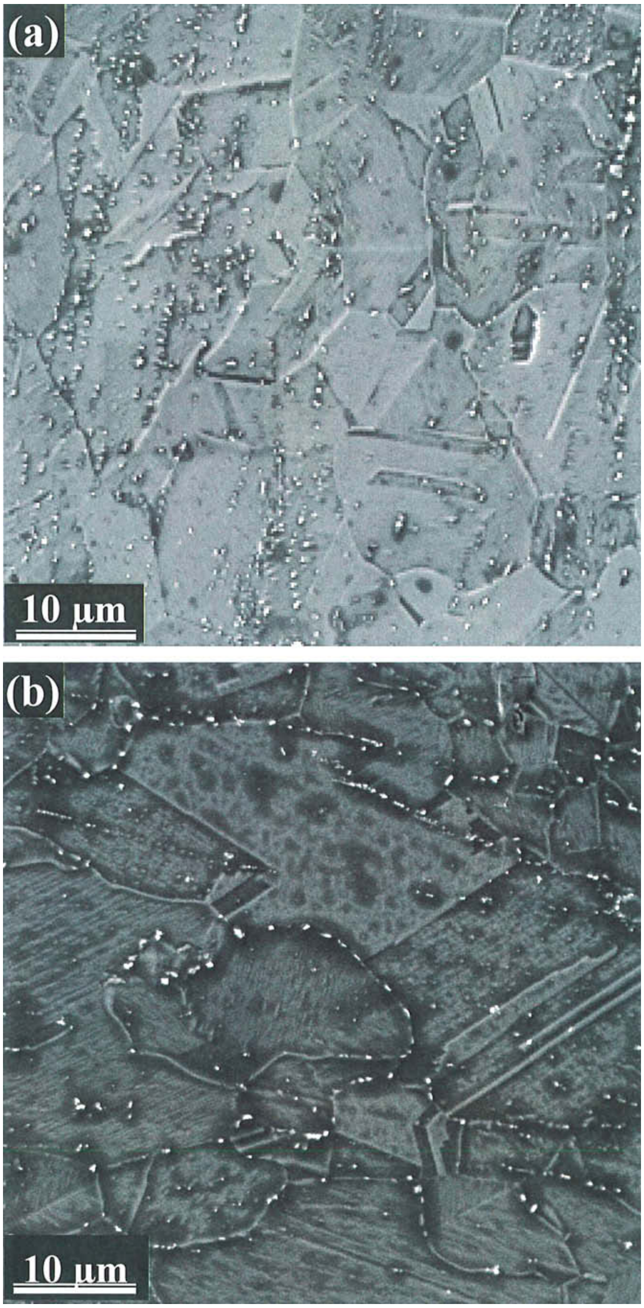

Fig. 1. SEM micrographs of studied Alloy 600 heats: (a) NX2650 heat and (b) NX3332 heat. Micrographs show a majority of intragranular carbides in the first case and rather predominant intergranular carbides in the second.

water used in the tests contained 1000 ppm B (weight) as boric acid (H_3BO_3), 2 ppm Li (weight) as lithium hydroxide (LiOH) and 30–50 cm^3 (standard temperature and pressure [STP]) H per kg of water, which was monitored with a Ag–Pd probe. NX 2650 U-bend exhibited IGSCC for 1538 h, and NX 3332 MA U-bend showed IGSCC for 11358 h.

2.2. Transmission electron microscopy (TEM) experiments

2.2.1. TEM sample preparation

Samples preparation was critical for the present work since oxides formed at crack tips and along crack walls had to be preserved against any alteration or contamination during mechanical polishing and ion milling. Thus, U-bends were first vacuum-impregnated in a low viscosity resin. This was done when U-bends were under load and cracks open. The section containing cracks was marked under the optical microscope and cut out. The obtained bar was then sectioned in thin foils of 0.4–0.5 mm in thickness. The thin foil with the well centred and extensively branched crack was selected and mechanically polished using tripod device. This was carried out on both sides using final 0.5 µm abrasive disc to achieve approximately 10–15 µm of thickness while preserving specimen surfaces parallel. Specimen was then mounted on a 3 mm-diameter copper grid to undergo ion milling. The thin foil was judiciously positioned in order to be pierced just below the *primary* crack (the deeper penetrated crack). This was achieved using Gatan© Precision Ion Polishing System (PIPS) with 4 keV and low-angle (±7°) argon ions. Final milling was performed at reduced beam energy (2 keV) and reduced incident angles (±4°) to remove most of the visible ion damage. Alternative ion milling – TEM observation was applied in order to obtain suitable thin areas of interest.

2.2.2. Advanced TEM characterization techniques

TEM observations and analysis were carried out on a 200 kV Tecnai F20 ST field emission gun microscope equipped with energy dispersive X-ray (EDX) device, scanning transmission electron microscopy (STEM) system, high angle annular dark-field (HAADF) detector and Gatan Imaging Filter (GIF). STEM-HAADF technique permits obtaining chemical contrast (Z-contrast) images. Thus, we can distinguish between oxidized and metallic zones. This was very useful for direct and rapid localization of boundary attacked zones especially when the specimen thickness or stress field made conventional TEM observations difficult.

EDX analysis using the brilliant and sub-nanometre probe produced by the microscope allowed local chemical investigation of oxides present at crack tips areas. In fact, in ideal conditions the minimum detectability of a chemical element by EDX microanalysis is <0.1 wt% of the analyzed volume but depending on experimental conditions this value can be higher. In our case all experimental conditions were optimized to maximize EDX sensibility especially for oxygen. However, element concentrations obtained from EDX analysis should be carefully interpreted since only approximate corrections were applied for O–Cr interference and oxygen X-ray absorption.

High-resolution transmission electron microscopy (HRTEM) images were acquired using a CCD camera. Local area fast Fourier transform diffractograms, equivalent to electron diffraction patterns, were exploited in order to determine structural and crystallographic characteristics of observed oxides.

A systematic combination of imaging techniques (HRTEM, HAADF) and chemical analysis (EDX) was applied in order to clearly identify oxides structure and composition.

3. Results

3.1. General microstructure features

TEM investigations were principally focused on the NX2650 heat. The NX3332 heat served uniquely to study the effect of intergranular precipitation on cracking rate. Thus, concerning the NX2650 heat, optical microscope examinations after corrosion test showed an extensive cracking with multiple crack initiation locations on the tubing outer surface (Fig. 2a). Cracks also exhibited extensive branching at their ends. In addition to the *primary* tip (deeper penetrating crack), several secondary cracks, more or less extended, are visible. Furthermore, apparently isolated crack segments coming from unseen secondary crack branches below or above section plane are also present.

Although the extensive cracks branching provided multiple possibilities of crack tips characterization, the ultrafine size of oxides formed inside crack required utilization of more resolved characterization methods. This was achieved using advanced TEM techniques which allowed distinguishing of two major boundary attacks: IGA and IGSCC. Furthermore, basing on propagation site and on nature of oxides formed at crack tip areas and along crack walls, SCC cracks were classified in different categories: *principal, secondary, twin boundary* and *transgranular*. Fig. 2b schematizes IGA attacks and the different encountered crack types. IGA and IGSCC were intensely investigated and results are detailed in the following sections.

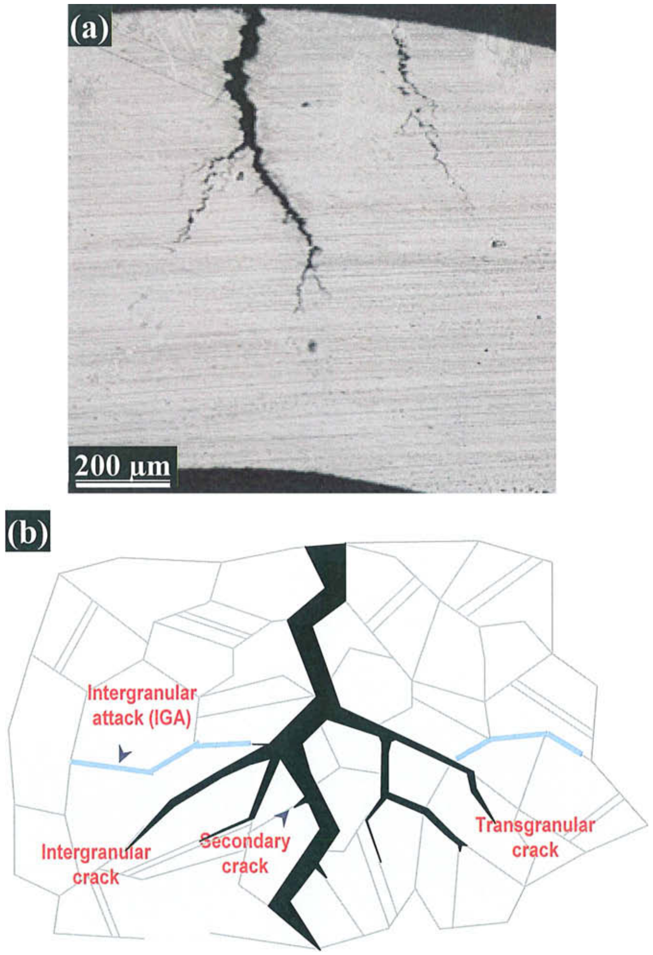

Fig. 2. (a) Optical microscope micrograph obtained on the cross-section of a tested NX2650 heat U-bend showing extensive cracking and (b) Schematic representation of IGA and different encountered crack types.

3.2. Intergranular attack (IGA)

It consists on narrow (10–15 nm) deeply penetrated oxidized zones along grain boundaries without the presence of cracking. Using STEM-HAADF imaging technique, it was possible to observe extended boundary attacked zones since the thin foil thickness effect is less crucial compared to the conventional TEM mode.

Fig. 3a shows an example of IGA with alternative oxidized zones (dark-contrast segments) and intermediate apparently intact boundary regions. Line-scan EDX analysis were realized through the oxidized zones. Thus, element compositional profiles revealed mainly Cr-rich oxide and nearly pure Ni metal regions existing side by side along the whole attacked zones (Fig. 3b). EDX analysis also revealed the presence of Ni-rich (Cr and Fe depleted) zone over 200–300 nm ahead of the oxidized zone tips. Beyond, the boundary exhibited the base alloy composition. Furthermore, no chemical change in the close vicinity of the attacked zones was detected and the neighbouring alloy matrix conserves the base alloy composition.

All these features are more clearly illustrated by Fig. 3c showing EDX cartographies performed on an oxidized zone tip area (framed zone in Fig. 3a). Thus, one can clearly see the side by side repartition of Cr-rich oxide and Ni-rich regions inside the attacked boundary, in addition to Ni enrichment of grain boundary ahead of the oxidized zone.

Fig. 4a presents a TEM micrograph obtained on an IGA region showing a fine-grained structure of the oxidized zone. In order to characterize oxides structures, lattice images were realized on different IGA zones (Fig. 4b) and fast Fourier transform (FFT) diffractograms of local areas (10 nm × 10 nm) were analyzed. Thus, Cr-rich oxides were clearly identified as Cr_2O_3 (see inset in Fig. 4b). Lattice images also clearly showed the side by side repartition of Cr_2O_3 oxides and pure Ni metal regions within the attacked zones. However, neither porosity was observed inside IGA zones nor ahead of the leading edge on grain boundary as reported by Thomas and Bruemmer [8].

Always by comparison with the latter study, the particular IGA features observed in the present case, notably the discontinuous aspect and the side by side repartition of Cr_2O_3 and pure Ni metal regions along the whole attacked zone, are probably due to the fact that IGA was observed parallel to its progressing direction. The discontinuous aspect of IGA could then result from the cutting of the IGA wave-shaped forehead by the thin foil planes as illustrated in Fig. 4c. Thus, besides confirming the predominance of Cr_2O_3 oxide at the IGA leading edge equally observed by Thomas and Bruemmer [8], TEM investigations revealed the wave-shaped form of the IGA forehead and the formation of an interesting Ni-enriched zone ahead of the attack tip. These microstructural features are supported by TEM observations carried out on SCC cracks.

3.3. SCC cracking

TEM investigations concerned only cracks where the protective resin remained intact after mechanical polishing and ion milling. Several tens of cracks were examined allowing identification of different types of cracks exhibiting different morphological and chemical characteristics.

3.3.1. Principal cracks

It was not possible to investigate oxides formed within the *primary* crack (the deeper penetrated crack) as it was largely open and the protective resin did not resist to the sample preparation causing alteration of oxides during ion milling. Fortunately, this was not the case of *principal* cracks where the protective resin remained most time intact. *Principal* cracks denote long intergranular cracks initiating from the *primary* crack. They are to be differentiated from

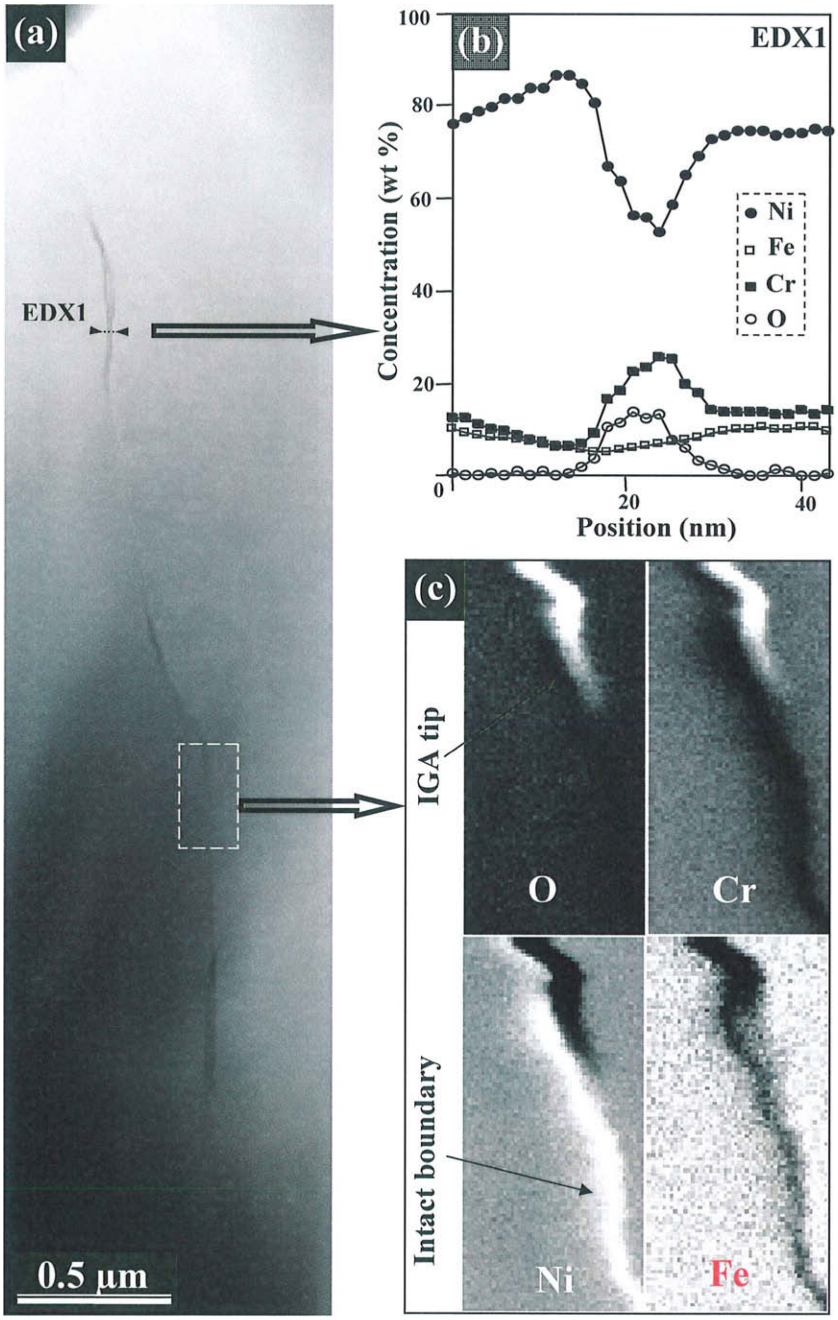

Fig. 3. (a) STEM-HAADF image of penetrative intergranular attack (IGA) showing oxidized zones (dark sections) separated by intact boundary segments; (b) compositional profiles obtained using fine-probe EDX analysis performed through an oxidized section showing that the latter are composed of Cr-enriched and near pure Ni metal regions sited side by side along the attacked zones and (c) EDX element cartographies performed on an IGA tip area (framed zone on (a)) showing the presence of Ni-enriched region ahead of the oxidized zone tip.

the very short ones called *secondary* cracks which will be detailed in the next section. Fig. 5a shows an example of a *principal* crack denoted crack 1 in the rest of the section. Since the image is slightly underfocused, this allows to clearly distinguish the crack tip/intact boundary border. Hence, one can observe the much narrowed crack tip area which extends over several tens of nanometres. When going inside the crack, the latter seems to be filled by nanocrystalline particles while others with larger sizes are lying on the crack walls. In crack open zones, the protective resin is also clearly visible even if it is torn in some regions. On the other hand, it was observed that some *principal* cracks tend to blunt at the first encountered triple point and often have a crack opened along a second grain boundary facet beyond the triple point. Fig. 5b shows an example of such cracks.

To determine nature of oxides formed inside *principal* cracks, EDX analysis using nanometric probe and high-resolution imaging were combined. Fig. 6a shows a STEM-HAADF image of crack 1. The chemical contrast allows to clearly distinguish between oxidized zones and intact boundary ahead of the crack tip. Line-scan EDX analyses were then performed through and ahead of the oxidized zones as indicated on the figure. The corresponding compositional profiles are presented in Fig. 6b, c and d, respectively. Thus, Ni enrichment (Cr and Fe depletion) of the boundary over approximately 100 nm just ahead of the crack tip was detected (Fig. 6b).

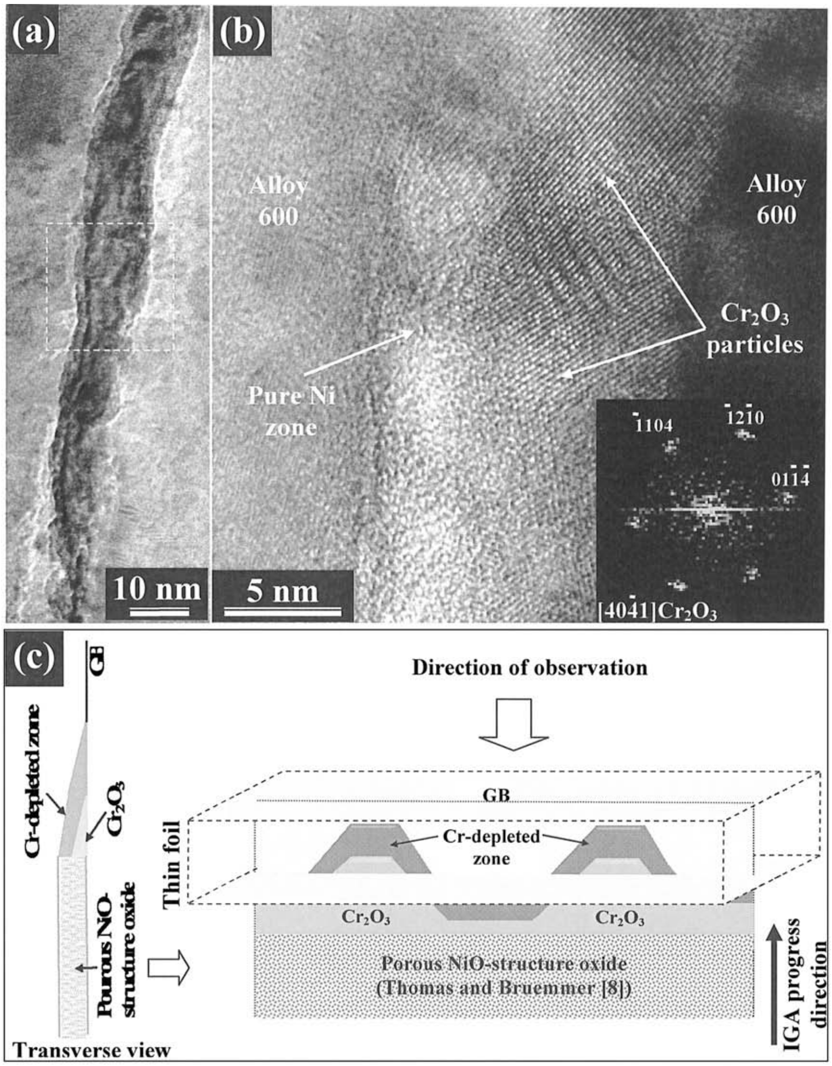

Fig. 4. (a) TEM micrograph obtained on IGA zone; (b) lattice image of framed zone on image (a) clearly showing the side by side repartition of Ni metal regions and Cr-rich oxides. The later were identified as Cr_2O_3 using fast Fourier transform (FFT) diffractogram (Inset image); and (c) schematic representations of IGA deduced from TEM observations. Left: Thomas and Bruemmer TEM observations [8]. Right: present direction of observation.

It is worth noting that no presence of oxygen has been detected in Ni-rich zones. Nevertheless, a presence of oxygen traces inferior to the EDX minimum detectability is not to be excluded. However, intergranular oxidation is excluded considering that oxygen concentration in NiO is superior to 27 wt% which would have been easily detected. Furthermore, as it will be seen below, HRTEM investigation did not reveal any presence of NiO-structure phase ahead of the crack tip.

At the tip area, compositional profiles clearly showed the presence of both Cr-rich oxide and nearly pure Ni metal regions distributed side by side (Fig. 6c). Far from the tip area, NiO-structure oxide with metal-atom ratio similar to the alloy seems to be predominant (Fig. 6d). Traces of S, Si and Al were also detected but were attributed to polishing compounds used in the sample preparation. Concerning the particles formed along the crack flanks, EDX analysis revealed element concentrations in agreement with $Ni(Fe,Cr)_2O_4$ oxides.

Crystallographic investigations of oxides were carried out using lattice images through the exploitation of the corresponding FFT diffractograms. Fig. 7a shows a lattice image obtained on the tip area of crack 1. One can easily distinguish the presence of two different lattice structures on each side of the tip. The indexation of FFT diffractograms of local areas highlighted the Cr_2O_3-structure of crystallites formed on the right side and the Ni-structure of those present on the opposite side, which is in perfect agreement with EDX analysis results. Cr_2O_3 oxides did not present any orientation relationship with respect to the alloy. Furthermore, Fig. 7a clearly shows that the crack tip terminates directly in the intact boundary and no altered zone exists just ahead of the crack tip as reported in the literature [8].

Fig. 7b presents a lattice image obtained at mid-zone area showing the formation along the crack flanks of NiO-structure oxide thin layer (~5 nm) owning parallel orientation with respect to the adjacent alloy matrix (Fig. 7b). The image also showed that the crack is filled with fine-grained particles identified in majority as NiO-structure oxides. On the other hand, exploitation of lattice images obtained on relatively big particles formed on crack flanks (Fig. 7c) allowed to clearly identify them as spinel $NiFe_2O_4$-structure oxides where Fe is partially substituted by Cr as was revealed by EDX analysis. Fig. 7d presents a schematic representation which sums up *principal* cracks features.

Finally, the high similitude of oxides structure and repartition between crack tip area and IGA leading edge seems to be characteristic of general intergranular attacks in Alloy 600 with or without

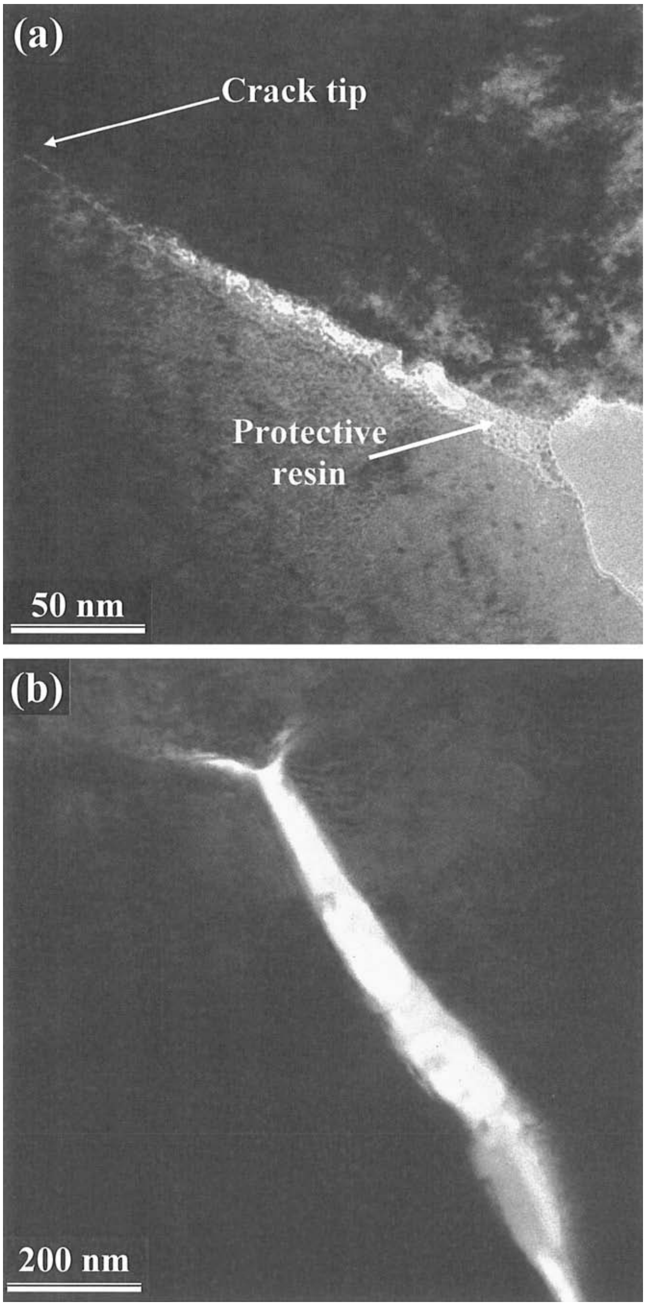

Fig. 5. (a) TEM micrograph showing a *principal* crack (crack 1) and (b) *principal* crack blunted at a triple point (crack 2).

cracking and may then provide valuable information about the mechanism of oxidation as it will be discussed in section 4.

3.3.2. Secondary cracks

These are short and sharp cracks initiated from long *principal* cracks as illustrated in Fig. 8a. It probably consists of stopped cracks. When observed using STEM-HAADF imaging mode, *secondary* cracks are easily recognizable owing to the tortuous shape and dark-contrast oxidized zone (~100–200 nm) present ahead of the crack tip (Fig. 8b). Inside the crack, the latter seems to be filled near the tip region. However, far from the tip area, deep insight on the image showed the formation of an oxide thin layer along open crack flanks. The layers seem to have complementary thicknesses, i.e. thickness of one oxide layer increased when the opposite oxide layer thickness reduced. This probably results from the fracture propagation through the initial oxide that filled the crack.

Line-scan EDX analysis performed through the oxidized zone ahead of the crack tip (EDX5) revealed, besides oxygen, chromium enrichment (~20 wt%), which is in agreement with Cr-rich oxide (Fig. 8c). When going inside the crack, at the filled zone near the crack tip area, element compositional profiles presented in Fig. 8d highlighted the formation of a Cr-rich oxide thin layer (~5–10 nm) along both crack flanks (see Cr concentration profile). Compositional profiles also revealed that oxide particles filling the crack are Fe-enriched and can be assimilated to $Ni(Fe,Cr)_2O_4$ oxide particles observed on *principal* crack flanks. Finally, no composition change of the matrix in the close vicinity of the crack flanks was detected. This was also the case of the grain boundary ahead of the leading oxidized zone. Fig. 8e presents a schematic representation which sums up *secondary* cracks features.

3.3.3. Twin boundary (TB) cracks

Twin boundary (*TB*) cracks exhibited a different shape and different oxides structure compared to *principal* cracks propagating along general boundaries. Indeed, *TB* cracks were unfilled and the tip area consisted on a porous fine-grained zone extending over approximately 150 nm before terminating on intact boundary (Fig. 9a and c). Fine-probe EDX analysis performed through the tip zone (EDX7) showed exclusive oxygen enrichment as illustrated by the compositional profiles presented in Fig. 9b. Thus, the exploitation of FFT diffractograms corresponding to local areas in this zone revealed that is about a NiO-structure oxide (see inset FFT diffractogram in Fig. 9c.

On the other hand, lattice images obtained along the open crack showed the presence of nanocrystalline particles forming a continuous layer on both crack flanks. These nanocrystals were equally identified as NiO-structure oxides (Fig. 9d). Other particularity of *TB* cracks was the absence of the Fe-rich oxide particles frequently observed on *principal* crack flanks and inside *secondary* cracks. Fig. 9e presents a schematic representation which sums up *twin boundary* cracks features.

Furthermore, it is worth noting that in some cases twin boundary cracks deviate from their initial itinerary to finish their propagation inside the grain. TEM and EDX investigations of such *transgranular* cracks revealed practically similar structural and chemical characteristics as twin boundary cracks, i.e. porous NiO-structure oxide at the tip area and fine-grained NiO-structure oxide on crack flanks.

Finally, all major microstructural features observed on IGA and on different IGSCC types are summarized in Table 2.

3.3.4. Effect of intergranular carbides on SCC susceptibility

Since Coriou studies [11], Alloy 600 is known to be susceptible to SCC in PWR primary water. In order to avoid this phenomenon, were used alloys with higher chromium content (Alloy 690 or Alloy 800). But another improvement was achieved by heat-treating to produce a high density of intergranular (IG) carbides. Understanding of the influence of IG carbides on IGSCC rate requires local investigation of carbides–cracks interaction. Hence, Alloy 600 heat with high density of intergranular carbides (NX3332 heat) was tested in the same conditions as the NX2650 heat and IGSSC was investigated.

Fig. 10a shows an optical microscope image obtained on the U-bend cross-section of the NX3332 heat. By comparison with the NX2650 heat (Fig. 2a), it is obvious that the presence of a high density of intergranular carbides in the NX3332 heat has considerably reduced the cracking rate. Indeed, only one crack initiation location at the outer tubing surface was observed. Furthermore, crack branching and penetration was strongly limited.

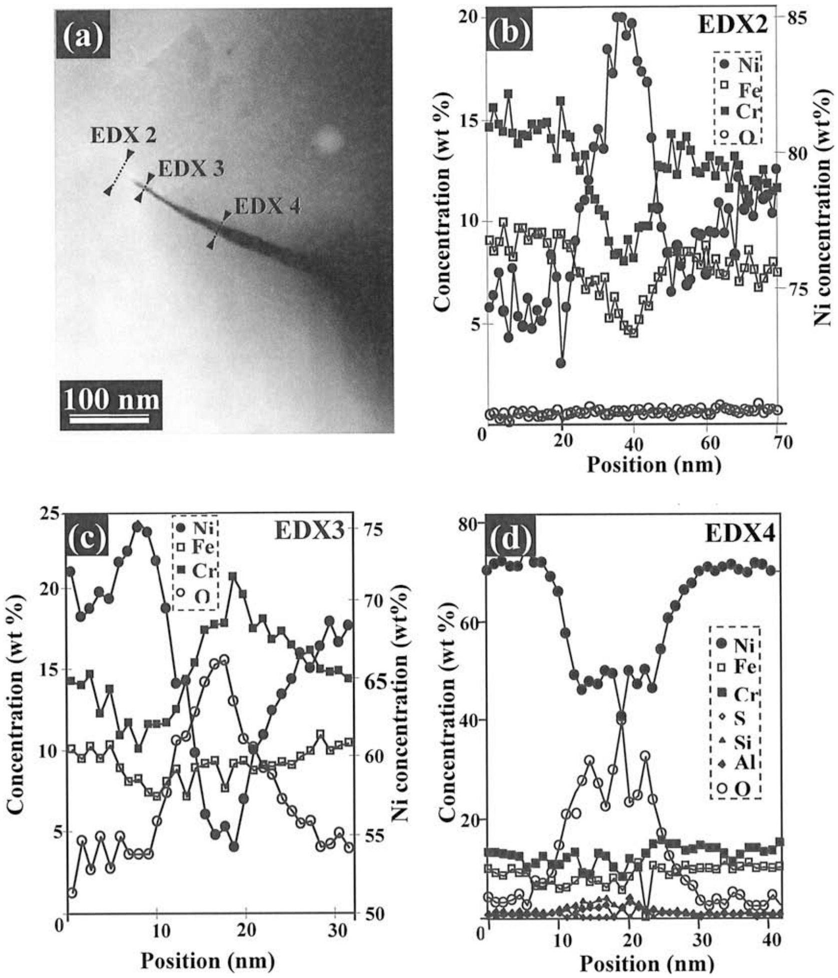

Fig. 6. (a) STEM-HAADF image of crack 1 with indication of EDX analysis locations; Compositional profiles obtained using fine-probe EDX analysis performed ahead of the crack tip (b); at tip zone (c) and at mid-zone area (d).

TEM investigations were carried out on several IGSCC cracks propagating near to intergranular carbides. In most cases, cracks propagation seems to be arrested by the presence of carbides as illustrated by Fig. 10b. Nevertheless, some SCC cracks succeed to go round the intergranular carbides (Fig. 10c) and continue their propagation causing either superficial oxidation or entire transformation of the intergranular carbide. Fig. 10d shows a STEM-HAADF chemical contrast image of oxidized IG carbide. The oxide layer appears as dark-contrast band of about 10 nm wide enveloping the attacked carbide. In some regions, the oxide penetrated inside the surrounding alloy matrix over several tens nanometres. Furthermore, an interesting bright-contrast zone located between the carbide and the oxide layer was observed. EDX analysis should confirm if it is about a different phase or simply an image defect.

Fine-probe EDX analysis was performed through the oxidized carbide (EDX8) and the obtained compositional profiles are reported in Fig. 11. Carbon is not presented because of contamination and absorption effects making unreliable its quantification. Analysis of element concentration profiles revealed that the oxide layer was enriched in chromium (~43 wt%) while the Ni content is probably originated from the alloy matrix regions crossed by the transmitted electron beam. EDX analysis also confirmed the Ni-enrichment of the bright-contrast band separating the carbide from the oxide layer observed on STEM-HAADF image of Fig. 10d.

High-resolution investigations performed on the attacked carbide (framed zone of Fig. 10d) allowed, via local area Fourier transform diffractograms analysis, to confirm the Cr_2O_3-structure of the thin oxide layer surrounding the carbide (Fig. 12a). The intermediate Ni-enriched zone was also clearly identified as pure Ni metal structure with orientation relationship with respect to the carbide. Fig. 12b presents a schematic representation which sums up oxidized intergranular carbides features. Finally, it is worth noting that all investigated intergranular carbides were identified as $Cr_{23}C_6$.

4. Discussion

4.1. Mechanism

The TEM observations permit to suggest a schematic sequence of cracking as shown in Fig. 13 [12,13]. Oxygen could diffuse by grain boundaries of polycrystalline oxide. Thus, oxides in crack or IGA do not seem to be a barrier for oxygen transport and oxygen could diffuse quickly from the surface up to IGA or cracks tips. Macroscopic stress could induce localized high strain rate in grain with the most favourable crystallographic orientation. This very high strain rate could generate a high default density near grain boundary at crack tip area and enhanced chromium diffusion by short circuit of diffusion at low temperatures of PWR conditions. Thus, chromium could diffuse quickly from the bulk to the crack tip. Then, chromium oxide could growth and embrittle the grain boundary. These hypotheses suggest that strain rate can be

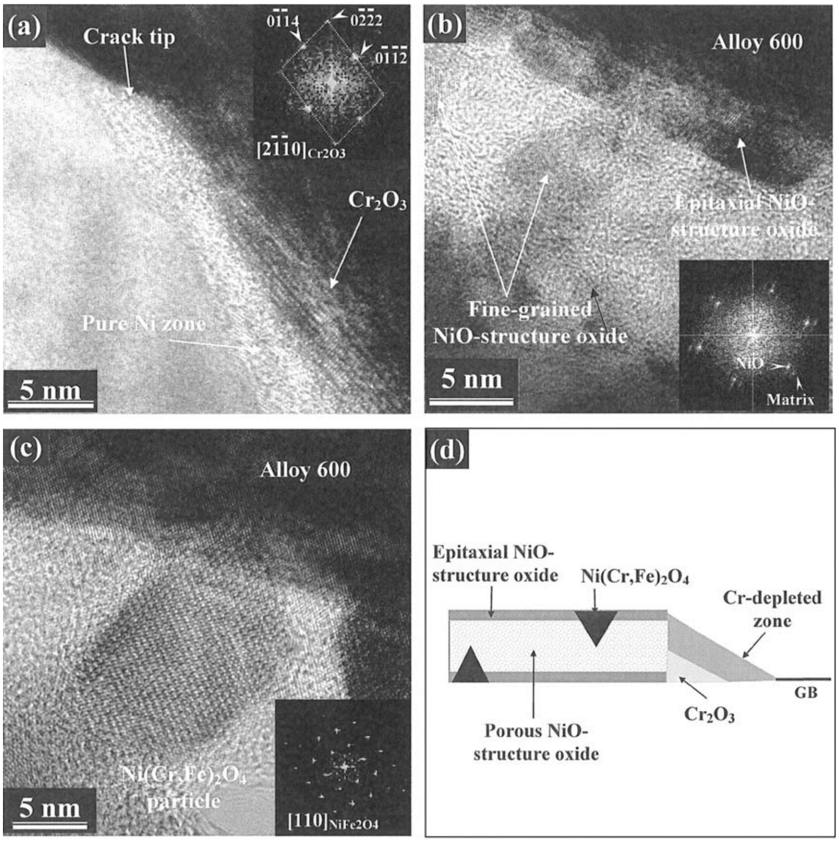

Fig. 7. Lattice images obtained along ⟨1$\bar{1}$0⟩ zone-axis (alloy) on: (a) tip area of crack 1 showing Cr_2O_3 oxide and Ni-rich metal regions; Inset image: FFT diffractogram of a local area image in the Cr_2O_3 zone; (b) nanocrystalline NiO-structure oxides filling the crack and epitaxial NiO on flanks; (c) Fe-rich particle formed on crack flanks. Inset image: FFT diffractogram confirming the $NiFe_2O_4$ structure such particles. (d) Schematic representation of the oxides nature and repartition in the *principal* cracks.

correlated to crack propagation kinetic by driving chromium diffusion kinetic.

IGA and *principal* cracks show chromium oxide associated to chromium depletion in alloy ahead of tip whereas *twin boundary* cracks and *transgranular* cracks show nickel oxide in the crack and at crack tip without depleted area in the alloy. Thus, it seems that chromium oxide associated to chromium depletion ahead of crack tip is characteristic of active cracks and therefore characteristic of IGSCC process. Without active process (*twin boundary* cracks and *transgranular* cracks case), observation would show neither chromium oxide nor depletion area in alloy.

This depletion seems to be caused by oxide formation. Indeed, kinetic transport of chromium in nickel is quite slow at this temperature [14]. Chromium diffusion at this temperature range (300–360 °C) could not be high enough to compensate chromium consumed by chromium oxide formation. Nevertheless, oxide formation and oxide growth within grain boundary need a constant chromium stream. Short circuit diffusion could explain this phenomenon.

The observation of NiO oxide in cracks could indicate favourable local oxidation conditions. This could be explained either by the presence of water filling the crack or by a low local hydrogen partial pressure, which information was not available. There is no experimental proof of its presence.

The results of the present investigation permit to support this cracking model [12,13] and discuss several features: continuous/discontinuous cracking nature, dissymmetric scheme of oxide repartition at crack tip and chromium carbide implication on IGSCC susceptibility.

4.2. Continuous/discontinuous cracking nature

In order to understand crack propagation mechanism, two hypotheses could be suggested:

1. *Crack propagation is a discontinuous mechanism*:

Oxide formation within grain boundary leads to grain boundary embrittlement, and then crack propagates beyond depletion area. Thus, oxide grows on crack walls. Oxide could grow at primary water/oxide interface; in this case, tensile stress generated by oxide growth on crack walls could lead to brutal crack propagation. In other cases, oxide could grow at oxide/alloy interface and could promote embrittlement of the grain boundary by mechanical feature degradation of the boundary.

2. *The second hypothesis involves a continuous mechanism with two propositions*:

– oxygen diffuses within the grain boundary and promotes chromium oxide formation. In this case, chromium oxide nodule could grow beyond crack tip.
– chromium diffuses through the grain boundary to oxide formation area (oxide/alloy interface). In this case, oxygen kinetic transport in chromium oxide and chromium kinetic transport in the grain boundary could influence the cracking propagation.

Another point that should be considered is the transformation of chromium oxide formed at crack tip when the crack propagates. Indeed, neither continuous nor discontinuous chromium oxide was observed in the crack far from the crack tip. This shows that chromium oxide has been transformed. Therefore, the repartition of

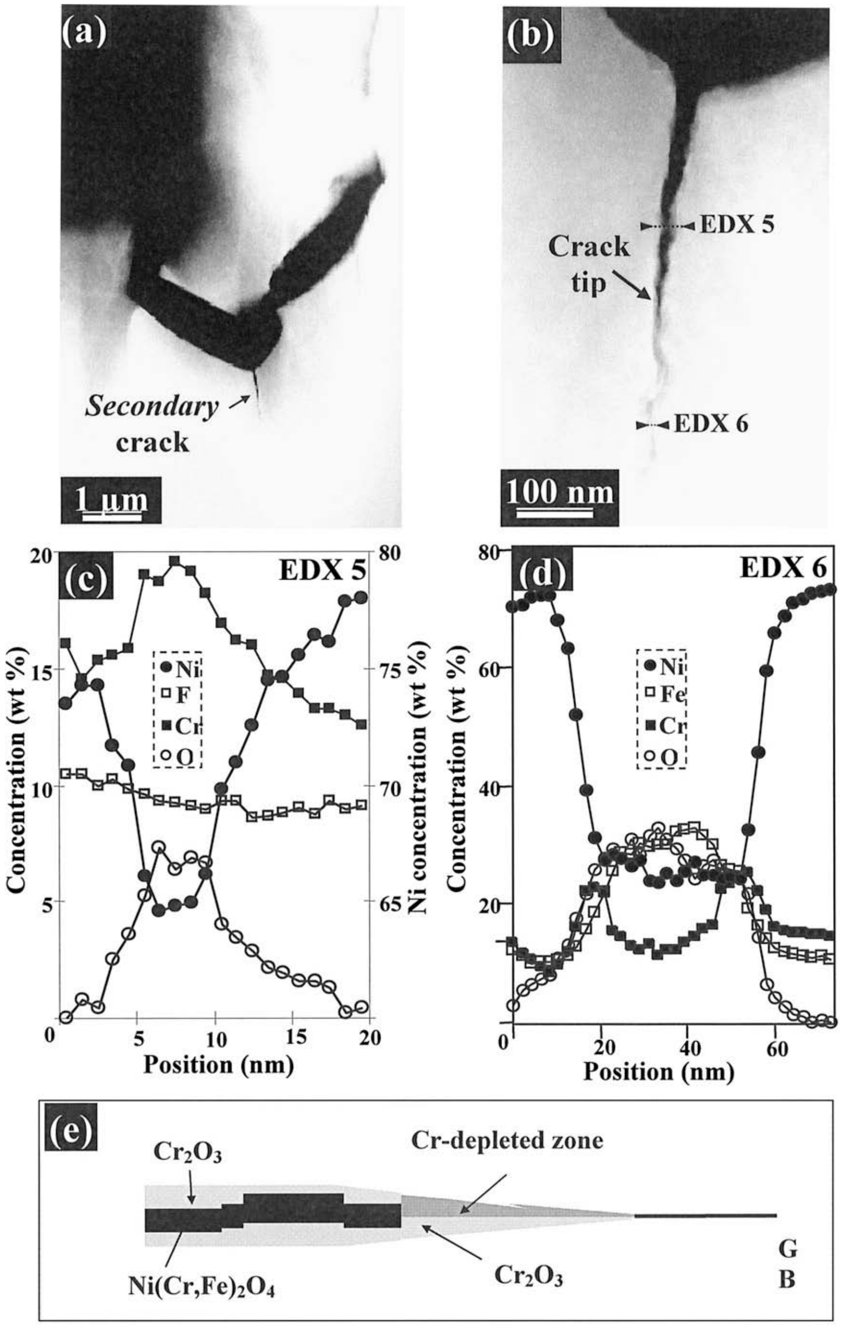

Fig. 8. (a) STEM-HAADF images obtained on a *secondary* crack; (b) Zoom on the crack area showing oxidized zone ahead of the crack tip; Compositional profiles obtained using fine-probe EDX analysis performed on the oxidized zone ahead of the crack tip (c) and through the open crack (d). (e) Schematic representation of the oxides nature and repartition in the *secondary* cracks.

oxides formed from chromium oxide on the crack sides could inform about cracking mode (continuous or discontinuous). $Ni(Cr,Fe)_2O_4$ particles were observed in the *principal* cracks. The fact that these spinels oxides consist of discontinuous particles could be the result of a discontinuous propagation of the crack.

STEM observations did not allow to confirm oxygen diffusion beyond crack tip within grain boundary. Indeed, even if penetrative intergranular attack composed of Cr-rich oxidized sections containing nearly pure Ni regions separated by Ni-rich segments is observed, nodules of oxide are not observed ahead of crack tip. A continuous mechanism with oxide formation at oxide/alloy interface and chromium diffusion from the grain boundary beyond crack tip is also possible. Deep IGA seems to support this hypothesis. Nevertheless, no continuous chromium oxide layer was observed in the crack.

4.3. Dissymmetric scheme of oxide repartition at crack tip

STEM observations show a dissymmetric aspect of crack tip. Indeed, chromium oxide at crack tip is associated with chromium depletion on one side of the crack and beyond the crack tip in the grain boundary. This dissymmetry could be explained by a preferential oxidation promoted by high default density (dislocations, etc.) localized in one grain adjacent to crack tip. Indeed, Schmidt factor could not be the same in both grains adjacent to crack tip. Thus macroscopic strain could induce localized high

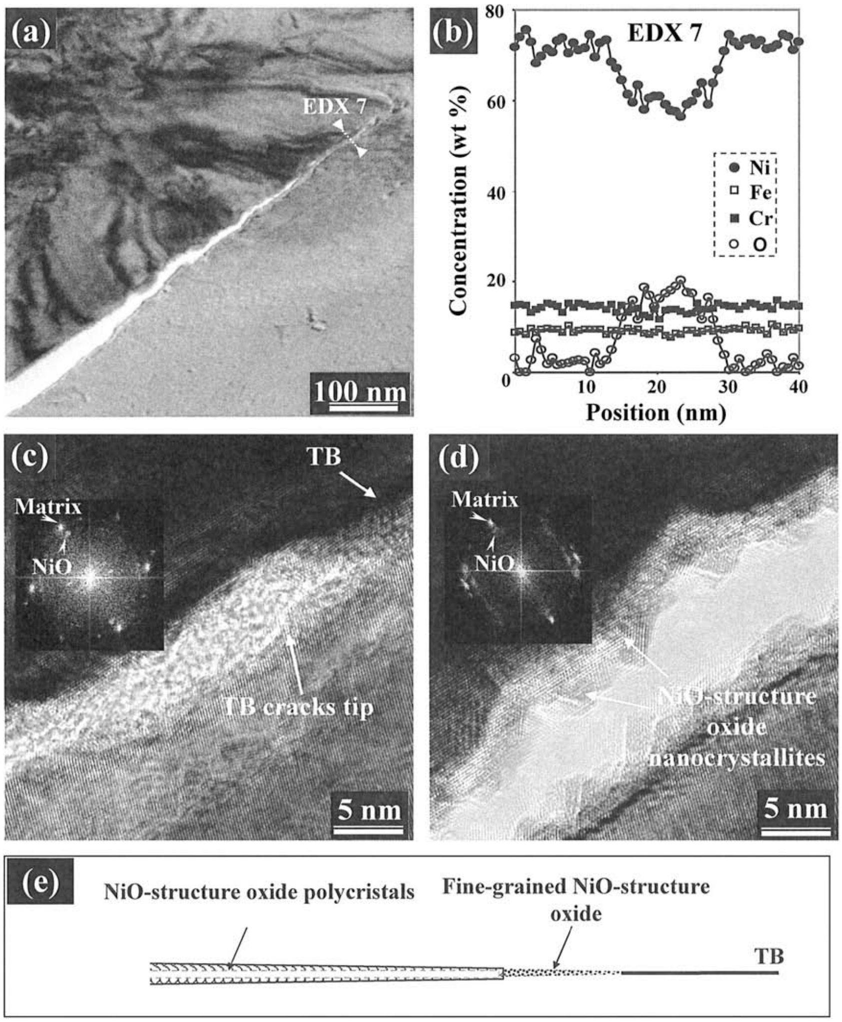

Fig. 9. (a) TEM micrograph of a *twin boundary* crack; (b) compositional profiles obtained using fine-probe EDX analysis performed through the tip area revealing predominant NiO-structure oxide; (c) lattice image of the tip area showing a very fine-grained structure identified as NiO-structure oxide (inset FFT diffractogram). (d) Lattice image showing nanocrystals formed along the crack flanks identified as NiO-structure oxides (inset FFT diffractogram); and (e) schematic representation of the oxides nature and repartition in *twin boundary* cracks.

strain rate in grain with the most favourable crystallographic orientation. This high strain rate could generate a high default density near grain boundary at crack tip. High default density like dislocations could promote oxide formation [15] and transport kinetic as suggested by Lozano-Perez [9].

Stress corrosion cracking mechanism involves a competition between oxidation and dynamic strain rate. Crack will blunt if the following conditions are encountered: oxidation rate is high enough, dynamic strain rate is high enough, the strain spread in a wide area, stress corrosion cracking will arrest. In our case, the strain area seems to be much localized ahead of the crack tip in the most favourable oriented grain. Thus the low width of the affected area is not sufficient to promote crack blunting.

4.4. Chromium carbide

According to Payne and Mc Intyre [10], $Cr_{23}C_6$ intergranular chromium carbides types do not promote SCC resistance, whereas Cr_7C_3 intergranular chromium carbides types promote SCC resistance. This could explain that carbides observed in the cracks are mostly $Cr_{23}C_6$ type. Nevertheless, all intergranular chromium carbides seem to inhibit the attack as evidenced by the duration

Table 2
Structural and compositional characteristics of oxides present in IGA and different crack types.

	Inside the crack (IGA)	On crack flanks	Tip area	Ahead of the tip
IGA	Nanocrystalline NiO-structure oxide [8]	–	Cr_2O_3 + Ni-rich regions	Ni-enriched zone
Principal cracks	Nanocrystalline NiO-structure oxide	$Ni(Fe,Cr)_2O_4$ particles + epitaxial NiO	Cr_2O_3 + Ni-rich regions	Ni-enriched zone
Secondary cracks	$Ni(Fe,Cr)_2O_4$ particles	Cr-rich oxide layer	Cr-rich oxide + Ni-rich regions	–
Twin boundary cracks	–	NiO-structure oxide nanocrystals	Nano-grained NiO-structure oxide	–
Transgranular cracks	–	NiO-structure oxide nanocrystals	Nano-grained and pourous NiO-structure oxide	–

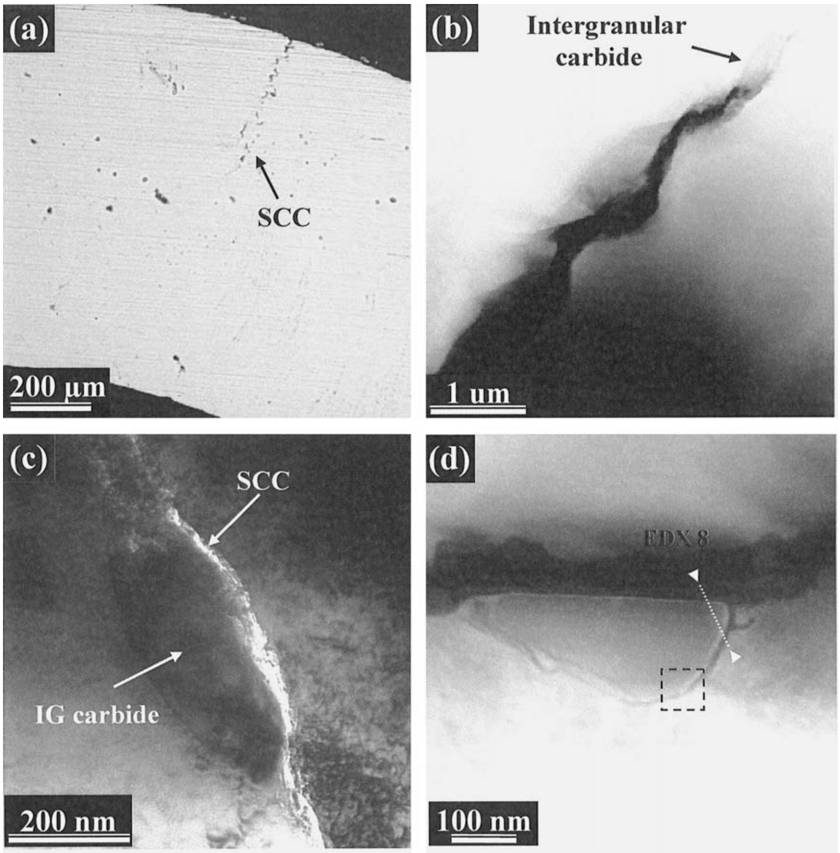

Fig. 10. (a) Optical microscope micrograph obtained on the cross-section of a tested NX3332 heat U-bend. (b) STEM-HAADF image obtained on a crack propagating close to intergranular (IG) carbide. (c) TEM micrograph of attacked IG carbide and intergranular crack going round it. (d) STEM-HAADF image of oxidized intergranular carbide where the oxide layer (dark crown) is clearly distinguished and separated form the carbide by a bright-contrast intermediate zone.

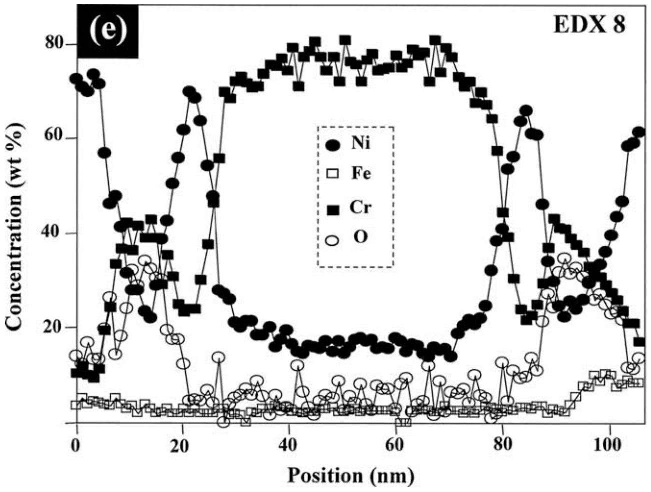

Fig. 11. Compositional profiles obtained using fine-probe EDX analysis performed through the carbide revealing that the oxidized zone is Cr-rich while the bright-contrast intermediate zone is Ni-rich.

necessary to obtain crack propagation (1538 h for NX2650 with low intergranular precipitation, 1135 h for NX3332 with high intergranular precipitation). Interaction with structural default like dislocations could explain this effect. Indeed, chromium carbides could stop dislocations. This could generate a very high default rate in the alloy near the chromium carbide. A high default rate promotes oxidation. Thus oxide could be formed on carbide and in some regions in the surrounding alloy matrix over several tens of nm as observed. In these conditions, tip geometry could be changed and stress factor decreased. Thus chromium carbide could promote SCC resistance. Nevertheless, the present work does not permit to discriminate $Cr_{23}C_6$ and Cr_7C_3 influence on SCC sensibility.

Interesting information revealed by the profiles is the presence of an intermediate Ni-enriched zone between the carbide and the oxidized zone. Epitaxial relations between Ni layer and carbide suggest that this layer is a chromium depleted zone in the carbide generated by oxide formation.

5. Conclusions

Nanoscale investigations of stress corrosion cracking (SCC) in Alloy 600 using advanced TEM techniques as HRTEM, EDX and STEM-HAADF revealed:

1. narrow intergranular attacks (IGA) with predominant Cr_2O_3 oxide and pure Ni metal regions at the leading edge area arranged in side by side layout. Ni-rich zone separate oxidized zone from intact grain boundary;
2. long *principal* cracks exhibiting following characteristics: (i) Ni-enriched (Cr depleted) zone ahead of crack tip; (ii) Cr_2O_3 oxides and Ni-rich regions arranged in side by side layout at tip area; and (iii) NiO-structure and $Ni(Cr,Fe)_2O_4$ oxides inside cracks and on cracks flanks;
3. short *secondary* cracks exhibiting following characteristics: (i) extended Cr-rich oxidized zone ahead of the crack tip; (ii) Cr_2O_3 oxide particles lying along crack flanks; and (iii) $Ni(Fe,Cr)_2O_4$ oxide filling open cracks;

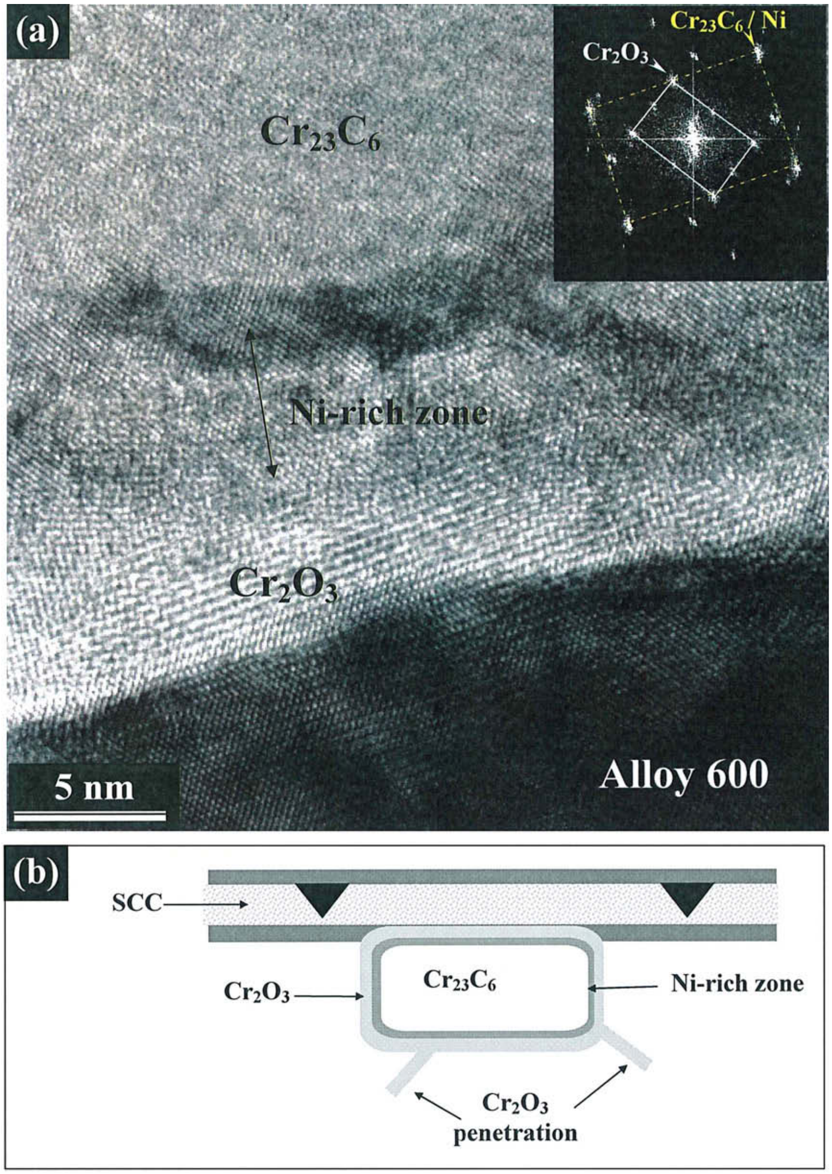

Fig. 12. (a) Lattice image of attacked IG carbide (framed zone in Fig. 10d). Inset FFT diffractogram reveals the Cr_2O_3 structure of Cr-rich oxide zones around the carbide identified as $Cr_{23}C_6$. Ni-rich intermediate zone is also identified as pure Ni metal structure with orientation relationship with respect to the IG carbide. (b) Schematic representation of the oxides formed on intergranular chromium carbide.

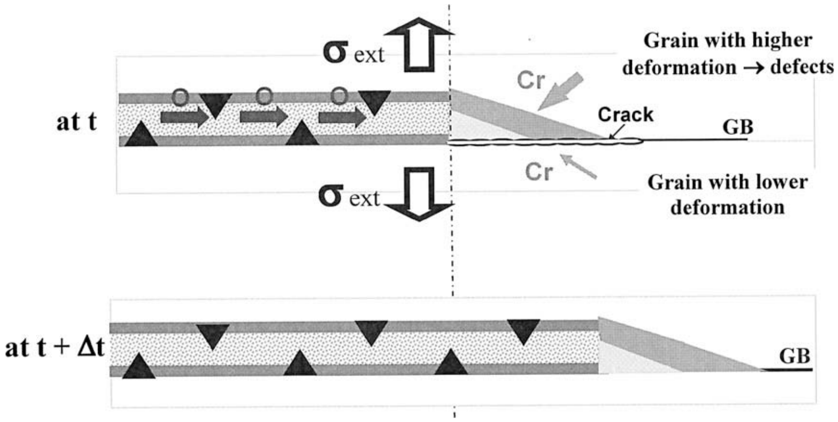

Fig. 13. Schematic representation of dissymmetric aspect of principal crack and schematic sequence of cracking proposed.

4. *twin boundary* and *transgranular* cracks with fine-grained NiO-oxide at tip area and on crack flanks;
5. interaction between intergranular carbide and stress corrosion crack showing oxidized intergranular carbides exhibited a Ni-rich zone between the carbide and the surrounding Cr_2O_3 oxide.

These results permit to discuss several features: continuous/discontinuous cracking nature, dissymmetric scheme of oxide repartition at crack tip and the chromium carbide role on IGSCC susceptibility. Furthermore, a model of cracking is proposed to explain primary water stress corrosion cracking of Alloy 600. Diffusion of oxygen through nanocrystalline oxide and diffusion of chromium enhanced by strain in grain boundary beyond crack tip seems to be the key steps of the proposed SCC mechanism.

Acknowledgements

The authors are grateful to Areva and EDF for financial support.

References

[1] S. Perusin, B. Viguier, D. Monceau, L. Ressier, E. Andrieu, Acta Mater. 52 (18) (2004) 5375.
[2] F. Delabrouille, B. Viguier, L. Legras, E. Andrieu, Mat. High Temp. 22 (3–4) (2005) 287.
[3] J. Panter, B. Viguier, J.-M. Cloué, M. Foucault, P. Combrade, E. Andrieu, J. Nucl. Mat. 348 (1–2) (2006) 213.
[4] F. Lecoester, J. Chene, D. Noel, Mat. Sci. Eng. A 262 (1–2) (1999) 173.
[5] P.M. Scott, An overview of internal oxidation as a possible explanation of intergranular SCC of Alloy 600 in PWRS, in: Proceedings of the Ninth International Symposium on Environmental Degradation of Materials in Nuclear Power Systems-water Reactors, Newport Beach, CA, 1999, p. 3.
[6] T. Magnin, F. Foct, O. De Bouvier, Hydrogen effects on PWR SCC mechanisms in monocrystalline Alloy 600, in: Proceedings of the Ninth International Symposium on Environmental Degradation of Materials in Nuclear Power Systems-water Reactors, Newport Beach, CA, 1999, p.27.
[7] J. Chêne, A.M. Brass, Metall. Mat. Trans. A 35A (2004) 457.
[8] L.E. Thomas, S.M. Bruemmer, Corrosion 56 (6) (2000) 572.
[9] S. Lozano-Perez, J.M. Titchmarsh, Mat. High Temp. 20 (4) (2003) 573.
[10] S.M. Payne, P. McIntyre, Corrosion 44 (5) (1988) 314–319.
[11] H. Coriou, L. Grall, Y. Legall, S. Vettier, Stress corrosion cracking of Inconel in high temperature water, in: 3rd colloque de métallurgie, Saclay, France, North Holland, Amsterdam, 1960, p. 161.
[12] P. Laghoutaris, C. Guerre, J. Chêne, R. Molins, F. Vaillant, I. De Curières, Contribution to model stress corrosion cracking of Alloy 600 in PWR primary water, in: Workshop on Detection, Avoidance, Mechanisms, Modeling, and Prediction of SCC Initiation in Water-cooled Nuclear Reactor Plants, Beaune, France, 2008.
[13] P. Laghoutaris, Stress Corrosion Cracking Mechanism of Alloy 600 in Pressurized Water Reactor Primary Water, PhD thesis, ENSMP, 2009.
[14] D.D. Pruthi, M.S. Anand, R.P. Agarwala, J. Nucl. Mat. 64 (1977) 206.
[15] M. Sennour, L. Marchetti, S. Perrin, R. Molins, M. Pijolat, O. Raquet, Mater. Sci. Forum 595–598 (2008) 539.